remote sensing

MDPI

Article

Integrating LiDAR, Photogrammetry, and Computational Fluid Dynamics for Wind Flow Simulations Around Existing Buildings

Richard Acquah [1,2,3,*], Edgaras Misiulis [4], Anna Sandak [1,2,3], Gediminas Skarbalius [4], Robertas Navakas [4], Algis Džiugys [4] and Jakub Sandak [1,2,3]

1 InnoRenew CoE, 6310 Izola, Slovenia; anna.sandak@innorenew.eu (A.S.); jakub.sandak@innorenew.eu (J.S.)
2 Faculty of Mathematics, Natural Sciences and Information Technologies, University of Primorska, 6000 Koper, Slovenia
3 Andrej Marušič Institute, University of Primorska, 6000 Koper, Slovenia
4 Laboratory of Heat-Equipment Research and Testing, Lithuanian Energy Institute, Breslaujos St. 3, 44403 Kaunas, Lithuania; edgaras.misiulis@lei.lt (E.M.); gediminas.skarbalius@lei.lt (G.S.); robertas.navakas@lei.lt (R.N.); algis.dziugys@lei.lt (A.D.)
* Correspondence: richard.acquah@innorenew.eu; Tel.: +386-70-257-208

Abstract: Integrating LiDAR and photogrammetry offers significant potential for ensuring the accuracy and completeness of the 3D models of existing structures, which are essential for several applications in the architectural, engineering, and construction (AEC) industry. This study has two primary objectives: the first is to demonstrate how LiDAR and photogrammetry complement each other, through the balance of LiDAR's structural accuracy with photogrammetry's rich texture data; the second is to validate the quality of the resulting mesh by using it for the CFD simulation of wind flow around a case study building. The integration method, though simple, is optimized to ensure high-quality point cloud registration, minimizing data quality impacts. To capitalize on the advantages of both manual and full point-cloud-based modeling methods, the study proposes a new hybrid approach. In the hybrid approach, the large-scale and simplified parts of the geometry are modeled manually, while the complex and detailed parts are reconstructed using high-resolution point cloud data from LiDAR and photogrammetry. Additionally, a novel region of constraints method (ROCM) is introduced to streamline wind flow simulations across varying scenarios without the need for multiple meshes. The results indicate that the integrated approach was able to capture the complete and detailed geometry of the case study building, including the complex window extrusions. The CFD simulations revealed differences in the wind flow patterns and pressure distributions when compared across different geometry modeling approaches. It was found that the hybrid approach is the best and balances efficiency, accuracy, and computational cost.

Keywords: computational fluid dynamics; wind flow simulation; LiDAR; photogrammetry; 3D geometry reconstruction; computer-aided design

check for updates

Academic Editor: Ali Khenchaf

Received: 9 December 2024
Revised: 27 January 2025
Accepted: 28 January 2025
Published: 6 February 2025

Citation: Acquah, R.; Misiulis, E.; Sandak, A.; Skarbalius, G.; Navakas, R.; Džiugys, A.; Sandak, J. Integrating LiDAR, Photogrammetry, and Computational Fluid Dynamics for Wind Flow Simulations Around Existing Buildings. *Remote Sens.* **2025**, *17*, 556. https://doi.org/10.3390/rs17030556

Copyright: © 2025 by the authors. Licensee MDPI, Basel, Switzerland. This article is an open access article distributed under the terms and conditions of the Creative Commons Attribution (CC BY) license (https://creativecommons.org/licenses/by/4.0/).

1. Introduction

Creating accurate building exterior models in 3D is essential for several applications, such as the restoration of historic buildings [1,2], structural analysis [3], environmental monitoring [4,5], and urban planning [6,7]. One important urban planning approach is computational fluid dynamics (CFD), which is mainly used for analyzing various parameters, such as pedestrian comfort levels and dose modeling of the influence of precipitation

on building facades. For CFD simulations, a 3D model is required to have no overlapping mesh elements and to be free of void regions. To achieve these goals, traditional CAD (computer-aided design) 3D modeling of the building and other technologies like building information modeling (BIM) are commonly used. However, traditional CAD/BIM approaches often cannot capture the differences between the building as-projected and the building as-built due to adjustments during construction [8].

To address this limitation, emerging point-cloud-based 3D reconstruction techniques offer a promising way to model and analyze buildings as they are built. As-built 3D models provide a more accurate representation of the building's current state, allowing for refined and reliable simulations. Recent studies, such as [7], emphasize that using as-built models enables more precise simulations that reflect the true conditions of the building, which cannot always be achieved using simplified models [7]. Similarly, ref. [9] demonstrate the effectiveness of as-built 3D heritage city models in supporting numerical structural analysis, showing that high-resolution point cloud data can be crucial for assessing and simulating the structural integrity of archaeological remains. Their study emphasizes the importance of accurate and detailed models in ensuring that simulations align with real-world conditions, reinforcing the need for precise as-built 3D modeling approaches [9]. The most commonly used point-cloud-based 3D reconstruction approaches are 3D scanning, such as light detection and ranging (LiDAR) technology or photogrammetry.

LiDAR technology has evolved over the last five decades [10]. It uses light in the form of a pulse laser to measure the distance between the light source (the scanner) and object(s) of interest. It is used for several applications including making high resolution maps in several fields including building science [11], surveying [3], 3D mapping and scan-to-BIM [12], forestry [4,13], and geomorphology [5]. On the other hand, photogrammetry is an image-based 3D modeling technique. It involves capturing a series of overlapping images of the object of interest from different orientations. Images captured are processed using algorithms that allow for the corresponding 3D geometry to be estimated. Just like laser scanning, photogrammetry is a well-established technology. Though photogrammetry is an old concept, it has gained popularity for scientific analysis [14] and has constantly been under development for use within the AEC sector over the past few decades [14,15].

These technologies are used for the quick creation of precise 3D models of buildings and their immediate environment [16]. Integrating data from LiDAR and photogrammetry has been found to be useful for several applications across different fields of study [2,17–19]. One of the promising uses is for scanning the exterior of existing buildings. Integrating these technologies opens avenues for advanced applications, such as service life performance modeling, which requires high levels of detail and accuracy in assessing how environmental conditions (including moisture and UV exposure) affect certain materials (like wood) over time.

However, relying solely on either 3D scanning or photogrammetry introduces limitations that compromise the accuracy of 3D models for CFD simulations. LiDAR point clouds provide precise structural details but lack surface textures [20], while photogrammetry captures detailed textures but often results in distorted structures [21]. Integrating both methods addresses these shortcomings, producing comprehensive and accurate models essential for reliable CFD simulations [1,22,23].

Recently, there has been growing attention on using accurate point cloud data for these types of simulations. For example, ref. [24] used LiDAR point cloud data to successfully simulate indoor fluid flow in a simple, box-shaped house. Other researchers have also shown that point cloud data are effective for building digital models and creating computational meshes for simulations [25–28]. However, despite these advancements and

prospects, a unified approach that combines LiDAR, photogrammetry, and CFD for urban planning and building simulations has not yet been given enough attention.

In this article, we present an urban planning analysis framework that integrates LiDAR, photogrammetry, and CFD, enabling the creation of accurate and detailed 3D models of building exteriors and performing CFD analysis for urban planning purposes.

The defining features of this framework are the 3D geometry reconstruction from the point cloud data obtained by integrating LiDAR and photogrammetry data, the development of a novel region of constraints method (ROCM) for efficiently simulating multiple wind flow scenarios around buildings, and the implementation of a hybrid approach that combines manual CAD modeling with point cloud data. The ROCM approach allows for the use of a single computational mesh across various wind speeds and directions, significantly improving simulation efficiency and scalability compared to traditional methods. The hybrid approach leverages the strengths of manual and point cloud modeling, where large-scale and simplified features are modeled manually, while complex and detailed areas are captured using high-resolution point cloud data. This combination optimizes computational resources and enhances accuracy. A case study of a building with complex window projections was used to demonstrate the capabilities and advantages of the proposed framework.

This framework addresses key challenges associated with the generation of high-quality 3D models that can be used seamlessly for CFD analysis [29]. The integration of LiDAR and photogrammetry data enhances the accuracy of as-built models, capturing the true state of buildings [30].

The hybrid approach presented in this study is particularly relevant for contributions to modeling building geometries for emerging simulation approaches such as mesh-free CFD modeling [31], neural-network-based fluid flow simulations [32], and machine-learning-optimized fluid flow simulations [33] for improved accuracy and efficiency.

The framework is also beneficial for CFD-related applications that require a high level of design detail. These include case-specific applications, such as modeling the wetting distribution of driving rain [34], modeling the dose response of bio-based construction materials, and modeling aesthetic changes in bio-based materials under environmental conditions [35,36] .

2. Materials and Methods

2.1. Description of the Case Study Building

The University of Primorska Livade Izola Campus Building, located in Izola, Slovenia, spans approximately 57 m in length and 33 m in width with four levels. The building is located on sloped terrain, featuring a multi-level design that integrates with the local coastal Mediterranean landscape. The test building as illustrated in Figure 1a has a flat roof; the façade includes protruding windows and recessed areas made of concrete and glass. These features disrupt airflow, leading to localized turbulence and pressure variations which make it interesting for studying several fluid flow conditions like wind flow conditions and wind-driven rain distribution, as illustrated in Figure 1b. Microclimatic data were obtained from a weather station located 170 m from the test building.

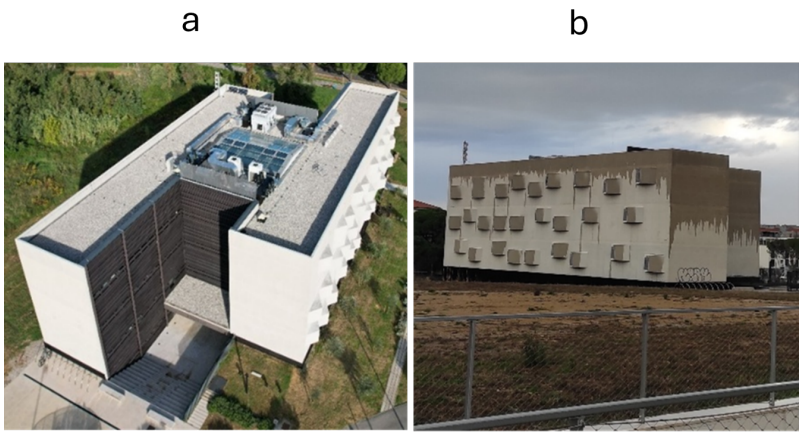


Figure 1. Case study building: the University of Primorska Livade Izola Campus Building (**a**) and wind-driven rain distribution (**b**).

2.2. Building Exterior Reconstruction from Point Cloud

The workflow chart of the processes involved in building exterior reconstruction from the point cloud is presented in Figure 2.

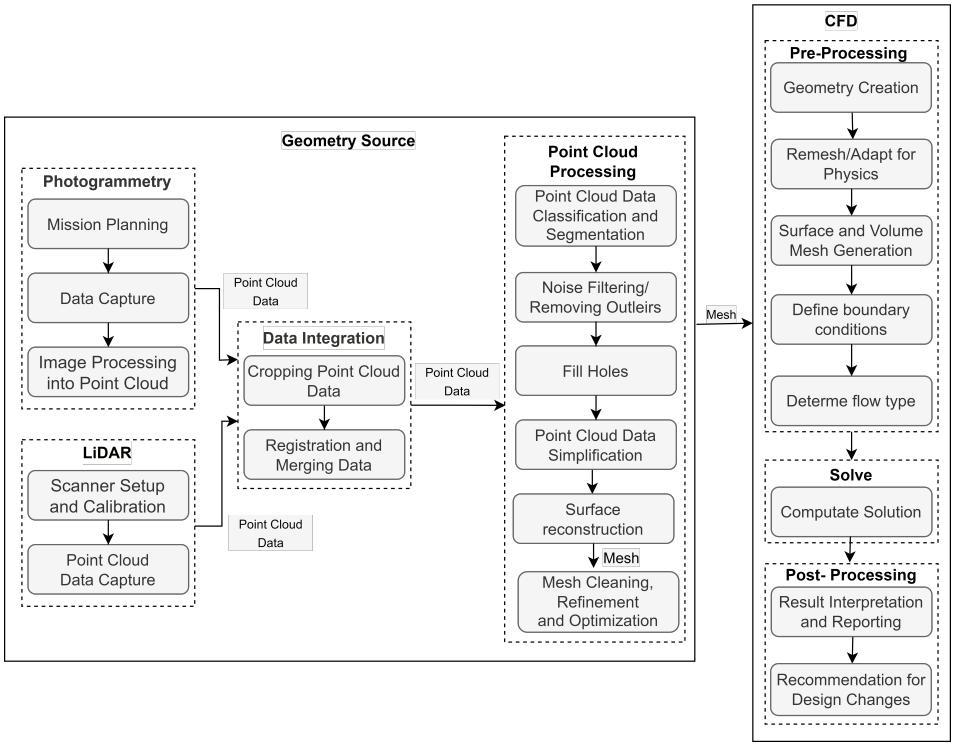


Figure 2. The workflow chart of the CFD modeling framework integrating LiDAR, photogrammetry, and CFD.

2.2.1. Point Cloud Acquisition

Terrestrial LiDAR and aerial photogrammetry were used to acquire point cloud data of the case study building. The acquisition of point cloud data using the LiDAR technology was performed using the Trimble X7 Laser Scanner, manufactured by Trimble Inc. in Sunnyvale, CA, USA. The photogrammetry data were obtained by taking high-resolution photographs of the building exterior from multiple angles using the DJI Mavic Air 2 drone, manufactured by DJI Innovations, based in Shenzhen, Guangdong, China. The photographs were processed using Pix4D photogrammetry software (v6.1) to create a 3D

point cloud of the building's surface. The Trimble X7 was chosen for its high scanning speed (500,000 points per second) and accuracy (2 mm at 10 m) to efficiently capture high-density point cloud data, that are essential for modeling the complex case study building features like window extrusions. This offers a maximum scanning distance of 80 m, with optimal accuracy within 60 m, and features a 360° horizontal and 282° vertical field of view, providing comprehensive coverage of building exteriors. Its automatic calibration ensures consistent data quality in urban environments.

Scan positions were strategically placed at 11 locations around the building to minimize occlusions and provide comprehensive coverage, ensuring that all building features, including hard-to-reach areas, were captured accurately. The Trimble X7 was set to the standard mode with a 7 min duration, achieving a point spacing of 4 mm at 10 m and capturing 125 million points per scan. Scanning was conducted during clear weather and midday hours to minimize environmental interference such as shadows or reflections.

The DJI Mavic Air 2 with its 1/2-inch CMOS sensor provides high-resolution (48 MP) images for aerial photogrammetry, capturing roof and window details from multiple angles. This efficiently fills gaps left by the terrestrial scanner, ensuring a comprehensive 3D model necessary for precise wind flow analysis and validating the hybrid approach presented in the study. Five drone flight missions were executed using the Litchi app (v4.26.2). One mission covered the entire perimeter of the building to capture a comprehensive view, while the four other missions were focused on each side of the building to capture detailed features.

The drone was programmed fly at an average altitude of 30 m with an average speed set at 5.0 m/s. The gimbal was adjusted to focus on the building's center (point of interest) with pitch angles varying between -15 and -42 degrees, depending on the height and details of each side, providing detailed capture of building features such as window extrusions, window projections, roof edges, and the facades. Each waypoint included a stop duration of 10 s for stable image acquisition, resulting in a total of 1017 images captured with an average overlap of 5 images per pixel.

2.2.2. Point Cloud Integration

All point cloud integration and processing tasks were performed using the open-source CloudCompare software (v2.12.4). The integration of point-cloud data from LiDAR and photogrammetry follows a semi-automatic workflow. These processes involved manually identifying common points or features in the datasets, such as corners and edges, and using these as reference points to accurately align the data within a common coordinate system using the CloudCompare alignment tools [37,38]. To enhance spatial accuracy, we utilized CloudCompare's iterative closest point (ICP) algorithm for fine registration, ensuring minimal discrepancies between datasets [39,40]. During integration, secondary data attributes such as RGB color, intensity values, and normals were preserved. RGB color from photogrammetry and the intensity from LiDAR were preserved for differentiation. Normals were computed and applied with the ICP algorithm to precisely align point clouds, resulting in a final RMS error of 2.85. Figure 3 illustrates the integration of the data from the two point clouds. Gray represents the LiDAR point cloud, while green represents the photogrammetry point cloud.

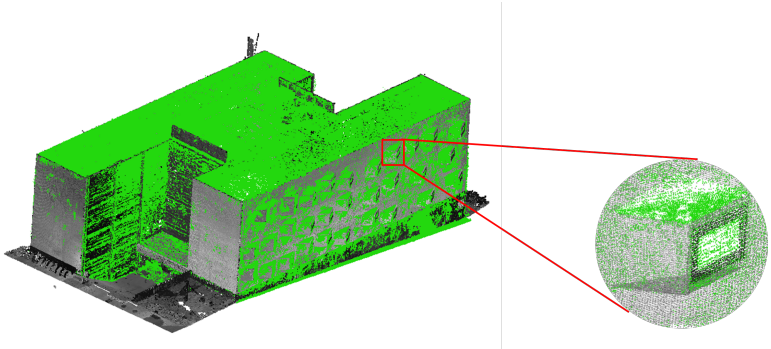


Figure 3. Integration of two distinct point cloud datasets for accurate 3D reconstruction. The gray points represent the LiDAR point cloud, capturing high-precision geometric data, while the green points represent the photogrammetry point cloud, detailing texture and visual features. Selected homologous feature points ensure precise alignment of the datasets.

2.2.3. Point Cloud Processing

The feasibility and accuracy of the CFD studies directly depend on the quality of the reconstructed surfaces. Therefore, three viable building exterior reconstruction methods (direct CAD, hybrid, and indirect) were implemented to fully analyze advantages and disadvantages of their use in CFD modeling for the scenarios of the wind's flow around the building.

Building exterior reconstruction methods:

Direct exterior reconstruction method

The building exterior was fully reconstructed from the point cloud data. The building exterior reconstruction began with the registered point cloud classification and segmentation, which are crucial steps towards point cloud simplification, leading to a more accurate surface reconstruction [41,42]. After the classification and segmentation step, the removal of outliers, noise filtering, and hole-filling procedures were performed on the segmented point cloud data. Following these procedures, point cloud simplification was performed using the octree subsampling approach [43]. After simplification, the screened Poisson (SP) surface reconstruction method [44] was used. The choice of this method was based on its ability to efficiently handle large datasets and its robustness to the noise which is often inherent in point cloud data [45]. Finally, the CloudCompare software (v2.12.4) was used to clean, refine, and optimize the resulting reconstructed building exterior for use in CFD simulations. This process aimed to achieve two basic CFD meshing rules proposed by [46] that include ensuring that there are (1) no void regions and (2) no overlapping mesh elements.

Indirect exterior reconstruction method

The building exterior was manually designed in COMSOL using computer-aided design (CAD) with a reconstructed surface mesh (obtained through direct method) as a reference. This method is the most used and standard way of modeling geometries for CFD simulation. Since this approach has been used and validated extensively in CFD studies, it was used in this study to validate the effectiveness of the two point cloud integrated geometry modeling approaches presented. This ensures that the integrated point cloud approaches (direct and hybrid) provide reliable and accurate as-built results.

Hybrid exterior reconstruction method

Large-scale building exterior features were designed using CAD with a reconstructed surface mesh (obtained through direct method) as a reference, while small-scale complex features of interest were fully reconstructed from the point cloud data. The data fusion (union operation) between building's global shape and details obtained from the point

cloud was not a trivial task and required many manual steps. Firstly, the mesh representing the global building shape and the mesh representing the details were imported into a single mesh. To minimize gaps and other probable nuances, the details were pushed about 0.1 m (which is about 10% of the length of window extrusion) inside the global shape. After this, union operation, which fuses meshes into a single mesh, was applied unsuccessfully; however, it provided a few locations were the mesh elements could not be fused. After removing the complex boundaries that caused the union operation to fail and replacing them with simpler boundaries, the union operation was successfully completed. Free triangular meshing and mesh adaption techniques, available in COMSOL, were applied to produce a smoother final surface mesh.

The reconstructed building exteriors obtained by using different methods with detailed window projections are presented in Figure 4. After the building exterior was reconstructed, it was centered on the origin of the global axis and it was enveloped by the "volumetric box", representing the external air volume forming the extended region of interest (eROI).

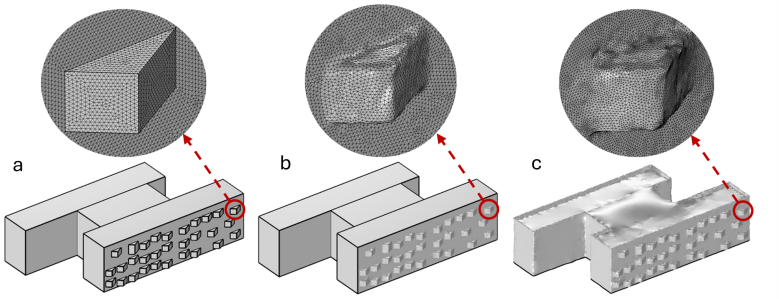


Figure 4. Building exteriors resulting from applying three different building exterior reconstruction methods: (**a**) indirect (CAD), (**b**) hybrid, (**c**) and direct (full point cloud).

2.3. CFD Modeling

The single-phase flow simulations of the wind flow around the test building were performed using COMSOL Multiphysics v6.0 software. The CFD simulation workflow, as presented in Figure 2, consists of three parts for results analysis: preprocessing, computation, and post-processing.

2.3.1. Rationale

When considering different wind flow modeling scenarios, the geometrical representation of the external air volume enveloping the building is usually of rectangular cuboid shape and is rotated in such a way that the wind flow direction is normal to one of the cuboid surfaces. The problem with this approach is that, for every wind flow scenario where the wind flow direction differs, a new geometrical representation and new computational mesh must be generated. In cases when the building exterior is complex, this could greatly impede the analysis, as automatic mesh generation might fail in some configurations, which then require time-consuming manual mesh editing.

To overcome this limitation, we propose a point-wise constraint (region of constraints method (ROCM)) approach that, when implemented, needs only one geometrical representation and, therefore, only one computational mesh. The drawback of this approach is that a single mesh must be generated taking into account all different wind flow speeds and directions of interest. If no prior information is available about the wind flow conditions, then the computational mesh must be fine enough to resolve all the relevant wind flow features from all possible wind flow directions. In addition, the computational mesh will have more mesh elements and will require higher computing power; as for particular wind flow conditions, there will be a lot of space with overly dense mesh.

2.3.2. Geometry Preparation

A single geometrical representation of the external air volume enveloping the building was of a rectangular cuboid shape with the dimensions (width × length × height) 750 m × 750 m × 65 m. The geometrical representation allowed us to perform a physics-adapted mesh-generation step.

2.3.3. Computational Mesh Generation

Computational mesh was generated, while ensuring that it can resolve all the relevant features of the wind flow and taking into account different wind flow speeds and directions. This was achieved by ensuring that the wall lift-off parameter near the building exterior would be in the optimal range, which is from 11.06 to a few hundred.

2.3.4. Governing Equations of CFD

For fluid flow simulations, one of the most important criteria is the Reynolds number. This is the ratio of acting inertial forces to viscous forces within a fluid. With an increase in Reynolds number, the flow transitions from the laminar flow regime into transitional and finally into turbulent flow regimes. The evolution of fluid flow is well predicted by the Navier-Stokes equations, which represent Newton's second law for a continuous medium. These equations, together with sophisticated numerical modeling techniques, are used in the CFD simulations to predict the fluid flow fields.

One of the defining features of CFD simulations of the wind flow around buildings is the range of possible wind conditions, as the wind direction can change from 0 degrees to 360 degrees and the wind speed can range from 0 m/s to about 10 m/s, and even up to 100 m/s in the most extreme cases [6]. Additionally, the Reynolds number criterion for wind flow around buildings is mostly in the turbulent regime, further increasing the complexity of the problem.

Several practical modeling approaches can be considered, such as large eddy simulation (LES) and Reynolds-averaged Navier-Stokes (RANS) for the simulation of wind flow around buildings. LES simulations can capture transient flow features such as flow separation, recirculation, and vortex shedding in the wake. Despite these advantages, the main drawbacks are higher simulation complexity and much higher computational cost. Although there are many nuances regarding RANS simulations, it is currently the most standard practical approach used by both engineers and scientists. Therefore, in our CFD simulations, we chose to use the RANS k-epsilon model and to perform stationary studies. We assumed the wind flow to be an incompressible Newtonian fluid with a constant density, which, for the stationary case, resulted in the following equations:

The conservation of mass (continuity):

$$\nabla \cdot \mathbf{U} = 0 \tag{1}$$

The conservation of momentum:

$$\rho(\mathbf{U} \cdot \nabla)\mathbf{U} = \nabla \cdot \left[-p\mathbf{I} + (\mu + \mu_T)\left(\nabla\mathbf{U} + (\nabla\mathbf{U})^T\right)\right] \tag{2}$$

where ρ is the air density, $\mathbf{U}$ and p are the time-averaged air velocity and pressure, ∇ is the nabla operator, $\mathbf{I}$ is the identity matrix, μ is the dynamic viscosity, $\mu_T = \rho C_\mu \frac{k^2}{\epsilon}$ is the eddy viscosity, $(\cdot)^T$ is the transpose operator, $C_\mu = 0.09$ is the turbulence model coefficient, k is the turbulent kinetic energy, and ϵ is the turbulent dissipation rate.

These equations are closed by the well-known RANS k-epsilon Equations [47]. The k-epsilon model constants are taken from [47] and are listed in Table 1.

Table 1. CFD RANS k-epsilon model constants taken from [47].

Constant	Value
C_μ	0.09
$C_{\epsilon 1}$	1.44
$C_{\epsilon 2}$	1.92
σ_k	1.0
σ_ϵ	1.3

2.3.5. Constraints and Conditions

A proposed region of constraints method (ROCM) was used to prescribe various wind flow conditions. Using ROCM, the entire air volume, named as the extended region of interest (eROI), was separated into inside and outside regions, where the outside region fully enveloped the inside region. In the outside region, named the region of constraints (ROC), the wind flow conditions were prescribed as point-wise constraints. In the inside region, named the region of interest (ROI), the wind flow was simulated based on the fluid dynamics equations. The main advantage of the ROCM method is that the ROC can be rotated based on the wind flow direction, allowing changes in wind direction while preserving the geometry and mesh (Figure 5).

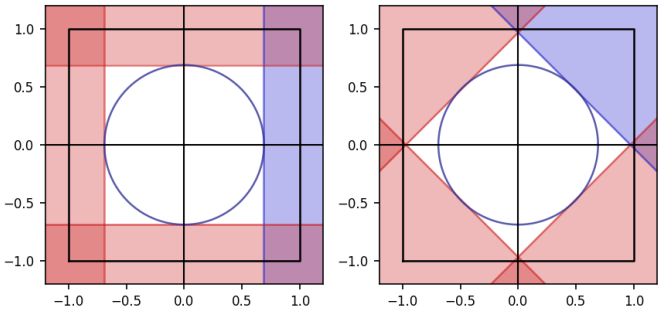


Figure 5. A visual example of the region of constraints method (ROCM). Considering that the constraints extend into the z coordinate, the inside of the black box corresponds to the eROI; similarly, the inside of the white box corresponds to the ROI, while everything in between the eROI and ROI corresponds to the ROC. The ROC region where the velocity is constrained ($ROC_{velocity}$) is depicted in red, while the ROC region where the pressure is constrained ($ROC_{pressure}$) is depicted in blue. (**a**) Unrotated ROC; (**b**) ROC rotated 45 degrees.

In our case, ROC was formed using four Euclidean planes. In general, the Euclidean plane is defined as follows: $ax + by + cz + d = 0$. Here, x, y, z are the spatial coordinates in the Cartesian coordinate system, and a, b, c, and d are coefficients. In our case, the d and c coefficients were set to zero, which made the Euclidean planes perpendicular to the z-axis, allowing analysis in 2D. Each of the four Euclidean planes was defined by a point $\mathbf{R}_i$ and a normal $\mathbf{n}_i$, where $i = 0, 1, 2, 3$ is the index for each point. All these four points were selected to be on a circle defined by Equation $x^2 + y^2 = (pL_{\text{eROI}})^2$ and separated by the angle of $\pi/2$, where L_{eROI} is the length of the side of the square, which forms eROI. The coefficient p was set to 0.69, thus ensuring that the ROI is always smaller than the eROI under any applied rotation. We note that $L_{\text{ROI}} = pL_{\text{eROI}}$, where L_{ROI} is the length of the side of the square, which forms the ROI.

The Euclidean plane inequality equations for the points and the corresponding normals are as follows:

$$\mathbf{n}_i(\mathbf{r} - \mathbf{R}_i) \geq 0 \tag{3}$$

The location for each point is defined as follows:

$$\mathbf{R}_i = L_{\mathrm{ROI}}\mathbf{n}_i \tag{4}$$

The normal vector for each point under rotation α is defined as follows:

$$\mathbf{n}_i = [\cos(\alpha + i\pi/2), \sin(\alpha + i\pi/2)] \tag{5}$$

The length ranges of the Euclidean planes were defined in such a way that none of them overlapped. Furthermore, using these four Euclidean planes and logical Boolean operators, the constraint regions highlighted in Figure 5 were formed: for velocity ($\mathrm{ROC}_{\mathrm{velocity}}$ in red color) and for pressure ($\mathrm{ROC}_{\mathrm{pressure}}$ in blue color). The Boolean functions were used in the domain point-wise constraint expressions: for velocity, $(u_{\mathrm{at\_boundary}} - u) \cdot \mathrm{ROC}_{\mathrm{velocity}}$; for pressure, $(p_{\mathrm{at\_boundary}} - p) \cdot \mathrm{ROC}_{\mathrm{pressure}}$. The outer air boundaries were prescribed to be open boundaries with no viscous stress and diminishing turbulent intensity and turbulence length scales, while the no-slip boundary condition was prescribed on the building exterior and on the ground.

The workflow of the proposed region of constraints method (ROCM) is shown in Figure 6. This method facilitates wind flow simulations across multiple scenarios by using a single mesh. This approach eliminates the need for multiple computational meshes and ensures efficiency in simulations, resulting in reduced manual labor and computational cost.

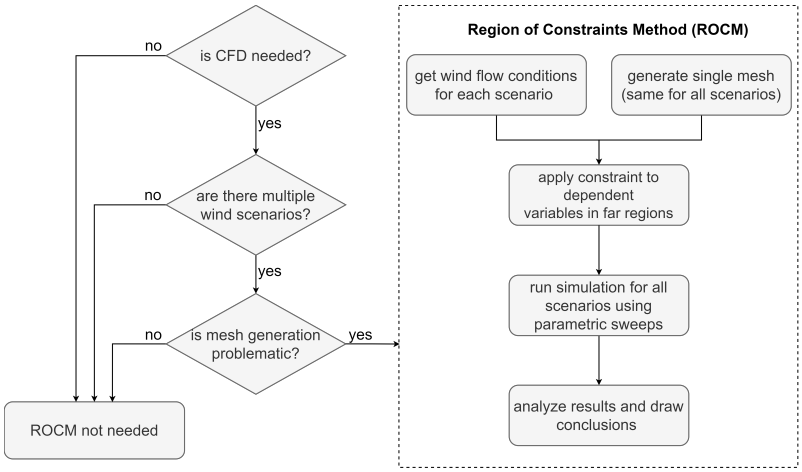


Figure 6. Flowchart illustrating the region of constraints method (ROCM).

2.3.6. Solver Settings

The CFD simulations were performed using the COMSOL Multiphysics v6.0 software. A steady-state approach was used to capture the average wind flow patterns around the building. The segregated solver was used where the pressure–velocity and turbulent variables were solved separately, allowing us to use a fast and memory-lean iterative solver. A state-of-the-art iterative generalized minimal residual method (GMRES) was used together with the smoothed aggregation algebraic multigrid (SA-AMG) preconditioner. The relative tolerance criteria was set to 1×10^{-3}, ensuring the good quality and the accuracy of the results.

2.3.7. Method Comparison

The comparison of the 3D reconstruction approaches was conducted based on eight weighted criteria. Each of the criteria was subjectively assigned a weight (0–10 scale). These weights were assigned based on expertise of authors and within the scope to represent its relative importance within the scope of this study. This allows for a qualitative and

quantitative assessment of the performance of each of the three modeling approaches was performed. The performance was evaluated using the following equations for weighted score, normalized score, and weight mean:

1. Weighted score ($w \times s$): The weighted score adjusts the raw score (s) based on the importance or weight (w) of the criterion. It is calculated using the following formula:

$$\text{Weighted Score} = w \times s \tag{6}$$

where:

- w: The weight assigned to the criterion, typically on a scale of 0–10, reflecting its relative importance.
- s: The raw score assigned to the assessment of each of the three approach in relation to the criteria, where:
  - Good = 0.1
  - Better = 0.5
  - Best = 1.0

2. Weight Mean: The weighted mean represents the overall normalized score for each approach, considering the relative importance of each criterion. It is calculated using the following formula:

$$\text{Weighted Mean} = \frac{\sum_{i=1}^{n} w_i s_i}{\sum_{i=1}^{n} w_i} \tag{7}$$

where:

- i is the index of each criterion, ranging from 1 to n.
- $n = 8$ is the total number of criteria.
- w_i is the weight assigned to the ith criterion, reflecting its importance.
- s_i is the score for the ith criterion.
- $\sum_{i=1}^{n} w_i s_i$ represents the total weighted score across all n criteria.
- $\sum_{i=1}^{n} w_i$ is the total sum of the weights for all n criteria.

Based on these equations the weight mean is computed as presented in Section 4.1.

3. Results

3.1. Point Cloud Capture and Integration

The point cloud data acquired from the LiDAR scan contained 131,583,758 points. This included the test building and its immediate surroundings. The point cloud data acquired from the photogrammetry process consisted of 21,382,781 points. The LiDAR data were reduced to 4,764,444 points and the photogrammetry data were subsampled to 3,530,600 points. The final point cloud dataset was 6,809,178 points through additional filtering to remove noise and irrelevant points.

As shown in Figure 7a, the LiDAR scan failed to capture the roof of the test building as well as top areas of the window projections of the test building. These are crucial features for the wind flow simulation of the test building and omitting it will influence the accuracy of the simulation results. The failure to capture these regions of the test building is due to the height of the test building and the lack of suitable vantage locations for the terrestrial LiDAR scanner. These are common limitations of terrestrial LiDAR in urban environments where tall buildings and obstructions prevent full coverage of the buildings in target. Similar challenges have been reported by [48–50].

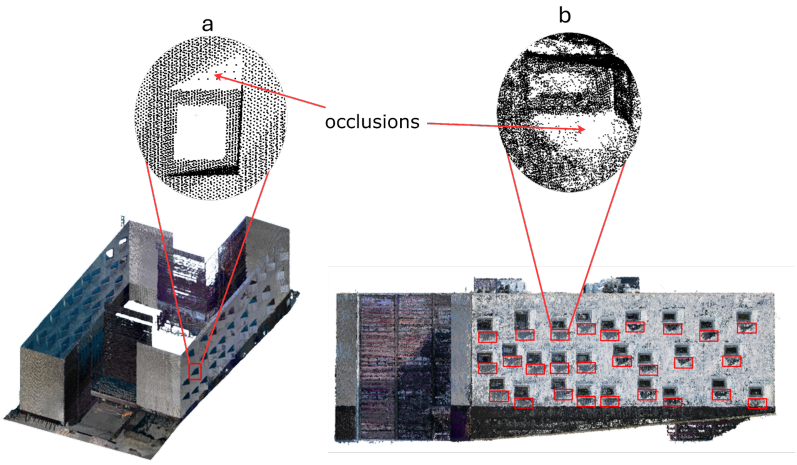


Figure 7. Point cloud data showing areas of the test building that the LiDAR (**a**) and photogrammetry (**b**) approaches were unable to capture (occlusions).

In Figure 7b, the point cloud data from the photogrammetry approach has gaps in areas below the window projections, which are also important for the wind flow simulation. This was because of limitation regarding drone camera positioning within the scope of the environment. This is a common challenge for photogrammetry applications where occlusion and shadows can reduce the quality of the resulting point cloud data [51].

Figure 8 shows the integrated point cloud data with normals, including a detailed close-up view of a window projection where the occlusions illustrated in Figure 7 have been resolved. The integration of point cloud data from both LiDAR and photogrammetry compensates for the limitations of each approach, resulting in high-resolution data and a more complete 3D geometry.

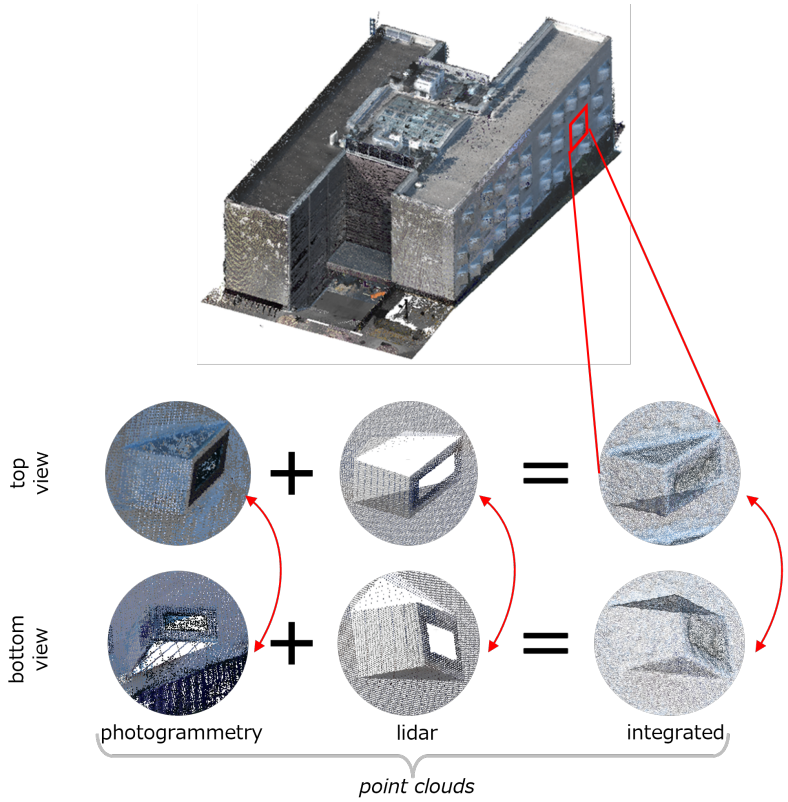


Figure 8. Integrated LiDAR and photogrammetry point cloud data showing top and bottom views of the same window.

Overall, the reduction in mesh density achieved a balance between computational efficiency and model accuracy, enabling effective analysis and simulation of the wind flow around the building while optimizing computational resources.

3.2. Mesh Quality Analysis

The mesh quality analysis was carried out by investigating key mesh properties including mesh resolution, quality metrics, mesh type, boundary layer treatment, and computational cost. The aim of this analysis was to compare the three different approaches to better understand the trade-offs between accuracy and computational efficiency and establish the optimal mesh strategy for achieving accurate and reliable CFD simulation results.

Figure 9 shows the histogram of the domain element quality for the entire geometry. The figure represents the histograms of the skewness of the mesh elements for each of the different geometry modeling approaches. It shows how element quality for all the elements in the mesh is distributed. The horizontal axis (x-axis) represents skewness, which measures the deviation of mesh elements from their ideal shape, ranging between 0.0 and 1.0. A value of 0.0 (far left) represents degenerated elements that are highly distorted and can negatively impact simulation accuracy, while a value of 1.0 (far right) indicates high-quality elements that align closely with the ideal shape, ensuring better simulation stability and accuracy. Generally, the more the histogram distribution tends to the right, the better is the mesh quality. Elements that are aligned more to the left are generally classified as degenerated elements. These elements can cause problems including element intersections and negative volumes. These often result in non-convergence of the numerical solver. The vertical axis (y-axis) on the other hand represents the number of elements of similar quality [52]. Since most of the elements stay in the higher quality range across all the three different geometry modeling approaches, the histograms depict an overall acceptable quality of the meshes.

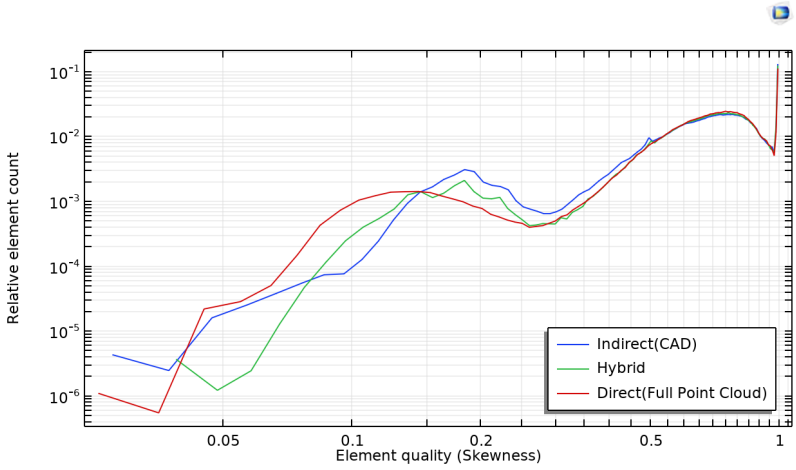


Figure 9. Comparison of element quality (measured by skewness) for three different geometry remodeling approaches: indirect (CAD-based mesh), hybrid (combination of point cloud and CAD), and direct (full point-cloud-based mesh). The histograms illustrate the distribution of element skewness, with lower values indicating better element quality.

For a detailed analysis of Figure 9, the graph is grouped into 4 skewness bins. These include 0.0–0.15 (1st bin), 0.15–0.3 (2nd bin), 0.3–0.5 (3rd bin), and 0.5–1 (4th bin). The 1st bin represents the region with poorly shaped, highly distorted mesh elements. In this region, the direct (full point cloud) accounts for the highest relative count of low quality elements. The indirect approach (CAD) generates the fewest distorted elements in this bin (0.0–0.15). The hybrid approach performs moderately among the three approaches. In the 2nd skewness bin, the element quality is better that the 1st. In this bin, the indirect (CAD)

approach produces the most elements, indicating a focus on moderate-quality meshes. Just like the 1st bin, the hybrid method demonstrates a more balanced performance with fewer elements compared to CAD but more than the direct approach. The direct (full point cloud) method has the least element count in this range, indicating it prioritizes higher-quality elements. In the 3rd skewness bin, the indirect (CAD) approach generates the highest number of elements, maintaining its lead in producing moderately high-quality meshes. The hybrid and direct (full point cloud) methods closely follow. The hybrid approach slightly outperforming the direct method in element count and is generally again considered to be having a balanced performance. In the 4th bin, the graphs for all three approaches follow each other. This is interpreted as having comparable performance. Based on the data presented in Figure 9, the hybrid approach is considered to have the overall better balanced performance as confirmed by the mesh statistics data presented in Table 2.

Table 2. Mesh statistics for all three geometry modeling approaches.

Mesh Property	Indirect (CAD-Based Mesh)	Hybrid (Combination of Point Cloud and CAD)	Direct (Full Point-Cloud-Based Mesh)
Total Number of Elements	1,216,249	1,190,767	1,314,506
Minimum Element Quality	0.023	0.034	0.021
Average Element Quality	0.694	0.702	0.701
Element volume ratio	1.985×10^{-7}	1.951×10^{-7}	2.395×10^{-7}
Element surface area (m^2) [only building exterior]	0.14	0.14	0.11
Mesh volume (m^3)	3.655×10^{7}	3.655×10^{7}	3.655×10^{7}
Number of Boundary Layers	5	5	5
Computational Time (hours)	1 h 31 min 54 s	1 h 37 min 5 s	2 h 39 s

Table 2 is an analysis of mesh statistics derived from different approaches: direct (full point-cloud-based mesh), indirect (CAD-based mesh), and hybrid (combination of point cloud and CAD). Though slight differences are observed, the mesh quality for all the different approaches are generally considered acceptable.

In comparison to all the approaches, the hybrid approach is considered the most balanced approach. It has the best minimum and average element quality, has a smaller element volume ratio, its exterior surface area equivalent to the Indirect approach and maintains a moderate computational time. The direct (full point cloud) approach has the highest element count, meaning that it has the highest computational cost. The indirect (CAD-based mesh) approach is the fastest and simplest. This makes it ideal for use cases where computational efficiency is a priority. However, its lower average quality suggests limitations for highly detailed simulations. In conclusion, the hybrid approach is considered to optimize both quality and efficiency.

3.3. CFD Simulation Results

Firstly, the CFD modeling was performed with manually prepared geometry (described in Section 2.3.3), which was optimized for CFD simulations. This was to show that our proposed modeling framework does provide the practically needed results for many different wind flow scenarios. Secondly, the CFD modeling was performed with both the point cloud and the hybrid geometry preparation approach (described in Section 2.3.3) to show that the modeling framework is general and can be used even with subpar quality geometry for CFD simulations with the advantage that the proposed framework reduces the amount of manual labor required for these types of simulations.

3.3.1. Wind Flow Patterns

The three different geometry modeling approaches led to distinct flow patterns around the building as presented in Figure 10. While trends in the general flow behavior were observed across all the three modeling approaches, the vortex formation and flow separations varied due to the differences in the surface details captured by each of the approaches. The fourth row of Figure 10 represents detailed results of the flow pattern of the CAD modeling approach (Figure 10(a4)), hybrid approach (Figure 10(b4)), and full point cloud approach (Figure 10(c4)). The white area represents the position of the test building.

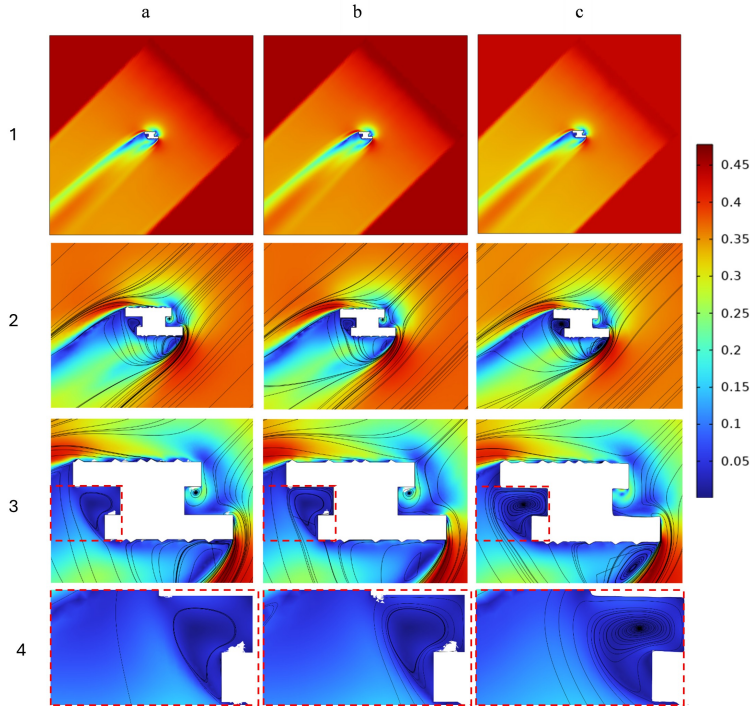


Figure 10. Far view (1st row), closer view (2nd row), zoomed-in view (3rd row), and detailed vortex analysis (4th row) of wind flow velocity magnitude (m/s) distributions around the building exterior (axes in meters) at 1 m from the ground. (**a**) Indirect method (CAD), (**b**) hybrid method, and (**c**) direct method (full point-cloud-based mesh).

The results from the CAD approach produced a small, stable and weaker vortex. This because the CAD modeling approach simplified the wall faces of the test building representing the faces with smooth flat surfaces. This results in delayed flow separations, less intense vortices, and minimal turbulence. The hybrid approach produces vortices that are larger and more pronounced. This indicates increase turbulence compared to the results from the CAD approach. The full point cloud captured the realistic uneven faces of the walls. Due to this, the results show a large, tightly packed vortex with darker, intense core, indicating high turbulence compared to the CAD approach.

It is expected that, when the manual 3D geometry modeling technique (CAD) is used, there is a high chance of omitting small details. This is particularly true for as-built geometrical modeling where the original geometrical drawings are not available. In cases like this, there can be oversimplifications when modeling the building geometry. This can result in a potential underestimation of the turbulence and localized flow patterns that might be crucial for certain applications such as modeling moisture decay at element intersections based on simulating wind flow influence on precipitation. In contrast, the point cloud reconstruction method and hybrid approach can result in a more accurate representation of the building's geometry, capturing local geometrical features and leading to more flow separations and turbulence. This approach offers a more realistic picture

of the wind flow around the very complex building geometries with implications for the accuracy of the results in real-world applications. The hybrid approach, which combines manual modeling with point cloud reconstruction, will capture the critical building details while maintaining a balance between computational efficiency and realism.

3.3.2. Pressure Distribution

The pressure distribution for the three different geometry modeling approaches as illustrated in Figure 11a–c show a general trend of high-pressure zones concentrated on the windward faces and a gradual transition to lower-pressure zones on the leeward side. However, a closer look at the results reveals variations due to differences in the surface details particularly at the roof. In the CAD (Figure 11a) and the hybrid (Figure 11b) approaches, the roof was simplified to a perfect flat surface neglecting the irregular as-built conditions. These simplifications resulted in a smoother and more uniform pressure profile over the roof in both cases. This is due to minimal flow disruptions and turbulence. In contrast, the full point cloud approach (Figure 11c) more accurately captures the as-built conditions, including the extruded edges of the roof. These introduce localized disturbances in the airflow which results in a more fragmented high-pressure zones at the roof.

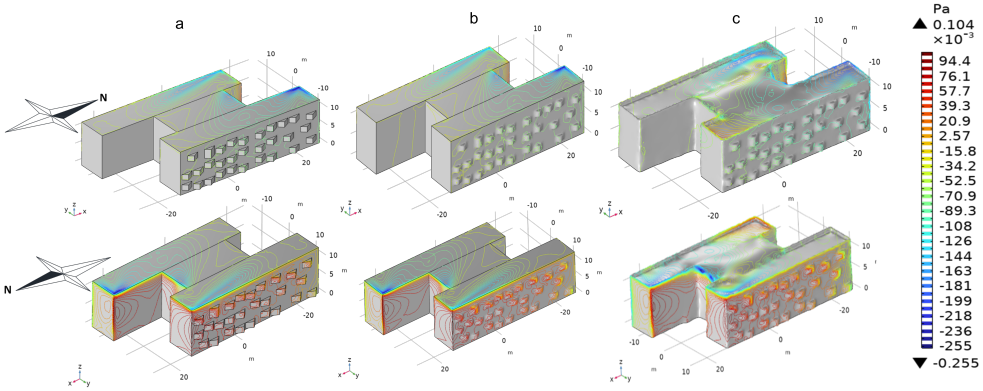


Figure 11. Pressure on building exterior walls for the three geometry modeling approaches. (**a**) Indirect (CAD-based mesh) method, (**b**) hybrid method, and (**c**) direct method (full point-cloud-based mesh).

4. Discussion of Results and Significance

The objectives of this study were to demonstrate how LiDAR and photogrammetry complement each other when capturing existing building geometries and to validate the quality of the resulting reconstructed geometry by using the mesh as input for CFD simulation of wind flow around the case study building. The results indicated that the point cloud integrated approach was able to capture the complete and detailed geometry of the case study building, including the complex window extrusions. The CFD simulations revealed consistent general trend in wind flow patterns and pressure distribution across the different geometry modeling approaches. However, variations in turbulence intensity and localized flow separations were observed, as presented in Figures 10 and 11. These variations identified highlight how important the influence of high geometric details on the accuracy of CFD results. For example, while the CAD-based method simplifies the geometry, this may lead to an underestimation of localized turbulence. The hybrid approach allows the modeler to captures essential details more accurately while maintaining efficiency. The full point cloud method despite its higher computational cost and higher total element count offer detailed and realistic representation of the building geometry. The results presented in this study give insight to modelers on choosing the most appropriate approach. For example, for high detail applications full point cloud will be suitable. However, to have control and balance

one modeling high detail and maintaining efficiency, the hybrid approach introduced in this study will be the appropriation.

4.1. Hybrid Approach in Relation to Results

As presented in Table 3, the mean values for manual modeling (0.50), point cloud reconstruction (0.47), and hybrid reconstruction (0.68) clearly indicate that the hybrid approach performs best overall. This is due to its ability to combine the strengths of both manual and point cloud modeling, achieving high accuracy while maintaining computational efficiency. The higher mean score demonstrates its superior performance across multiple criteria such as accuracy, flexibility, and adaptability, making it suitable for a wide range of projects.

The hybrid approach is particularly advantageous for complex and large-scale projects, as it enhances precision by using LiDAR and photogrammetry to model crucial details like window extrusions and roof variations. This ensures accurate wind flow simulations without requiring high detail throughout the entire structure, thus optimizing resources. By combining manual CAD for broader features and applying high-resolution modeling where needed, it reduces processing times and computational loads, maintaining accuracy and scalability. This adaptability allows the hybrid approach to efficiently handle diverse project scales and complexities, as shown in Tables 2 and 3.

Table 3. Comparison of 3D modeling and reconstruction approaches based on weighted criteria and normalized scores. Each criterion includes its assigned weight (0–10 scale) in brackets. The performance of each reconstruction method is described qualitatively. The Weight Mean represents the overall average score for each approach, calculated by summing the weighted scores for all criteria and dividing by the total weight.

Criteria (Weight)	**Indirect (CAD-Based Mesh)**	**Hybrid (Combination of Point Cloud and CAD)**	**Direct (Full Point-Cloud-Based Mesh)**
Detail and Accuracy (0.90)	High control but may miss complex details (Good)	Balance detail, accuracy, and control (Best)	Captures details accurately (Better)
Data Acquisition and preprocessing (0.80)	Low data acquisition needed (Best)	Balanced data management and preprocessing (Better)	Intensive data acquisition (Good)
Efficiency and Resource Requirements (0.80)	Time-intensive but minimal hardware needs (Best)	Efficient resource use (Better)	Resource-heavy, high computational needs (Good)
Potential for Automation (0.70)	Low automation potential (Good)	Moderate automation, efficient data processing (Better)	High potential with software advances (Best)
Technical Expertise Needed (0.70)	High CFD and geometry modeling expertise but no point cloud expertise needed (Best)	Requires CFD, geometry modeling, and point cloud expertise (Better)	Requires CFD, geometry modeling, and point cloud expertise (Better)
Scalability (0.70)	Limited by manual effort (Good)	High scalability, manual and automated methods (Better)	Highest scalability for complex projects (Best)
Flexibility and Adaptability (0.60)	Flexible for simple projects (Good)	Highest flexibility across project types (Best)	Adaptable to complexity, processing-intensive (Better)
Integration with CFD Tools (0.60)	Direct integration, potential additional effort (Better)	Ease of manual methods with detailed point cloud data (Best)	Conversion and optimization required (Good)
Weight Mean	0.5	0.68	0.47

4.2. Novelty of the Region of Constraints Method (ROCM)

The region of constraints method (ROCM) introduced in this study offers a significant advancement by enabling the simulation of multiple wind flow scenarios around buildings using a single computational mesh. This eliminates the need for generating new meshes for each scenario, significantly reducing manual labor and computational time. By utilizing predefined constraints, the ROCM efficiently accommodates various wind directions and speeds, making it suitable for urban-scale CFD applications where building geometries are often complex.

The key novelty of the ROCM is its balance between computational efficiency and simulation accuracy. Although an initial, comprehensive mesh is required to capture all potential wind conditions, this investment is offset by the method's ability to maintain a consistent mesh structure, avoiding the need for continuous reconfiguration. This approach is particularly effective in urban environments with irregular building shapes that challenge conventional meshing techniques. However, the comprehensive initial mesh can lead to higher initial computational demands if wind flow scenarios are not clearly defined, potentially increasing computational overheads. Future work could optimize the ROCM further by integrating adaptive meshing techniques to adjust mesh density dynamically, enhancing efficiency based on real-time simulation needs.

5. Conclusions

In order to model accurate 3D geometries of existing building and to simulate the wind flow around them, this study demonstrated the integration of LiDAR, photogrammetry, and CFD. As presented in Table 3, the study introduces hybrid as-built geometry reconstruction (which combines high-resolution point cloud data with manual CAD modeling) and the region of constraints method (ROCM) for wind flow simulation. The study concludes that the hybrid reconstruction approach is a better way of modeling as-built building geometries in situations where a balance between detail and efficiency is required. The region of constraints method (ROCM) presented in this study improve accuracy and efficiency by enabling the use of a single computational mesh for various wind scenarios. These improve building design optimize and enhance urban planning. This study not only advances wind flow simulation techniques but also establishes a background for point-cloud-based modeling of factors such as moisture, material temperature, and solar radiation, which are relevant for advanced applications such as service life performance modeling.

However, it is important to acknowledge the assumptions made regarding wind flow conditions (incompressible Newtonian fluid with a constant density). This could limit the applicability of the results in some real-world cases. Furthermore, the workflow presented in this study require the use of already existing software and manual intervention for point cloud integration and geometry reconstruction. This can be time-demanding and may introduce inefficiencies.

These limitations highlight areas that require improvement in the future. This include developing case specific software and tools to automate and streamline the workflow to better accommodate complex urban environments. Expanding the framework's capabilities for other wind flow conditions can improve its applicability across various domains within the AEC industry. In addition, findings from this study can be improved to enhance the modeling of wind-driven rain and modeling the appearance changes in wood deck construction and facades which requires high level of design detailing.

Author Contributions: Conceptualization, R.A., E.M., A.S., J.S., R.N., G.S. and A.D.; Methodology, R.A., E.M. and J.S.; Validation, R.A., E.M. and J.S.; Formal Analysis, R.A. and E.M.; Investigation, R.A. and E.M.; Resources, R.A., E.M., A.S., J.S., R.N., G.S. and A.D.; Data Curation, R.A. and E.M.;

Writing—Original Draft Preparation, R.A. and E.M.; Writing—Review and Editing, R.A., E.M., A.S. and J.S.; Visualization, R.A.and E.M.; Supervision, A.S., J.S. and A.D.; Project Administration, R.A., E.M. and J.S.; Funding Acquisition, R.A., E.M., A.S., J.S., R.N., G.S. and A.D. All authors have read and agreed to the published version of the manuscript.

Funding: This research was partly funded by WoodLCC, supported by ERA-NET Cofund Forest-Value: GA NO 773324 with national funders from participating countries.

Data Availability Statement: The original contributions presented in this study are included in the article. Further inquiries can be directed to the corresponding author.

Conflicts of Interest: The authors declare no conflicts of interest.

References

1. Gomes, M.G.; Tomé, A. A digital and non-destructive integrated methodology for heritage modeling and deterioration mapping. The case study of the Moorish Castle in Sintra. *Dev. Built Environ.* **2023**, *14*, 100145.
2. Alshawabkeh, Y.; Haala, N. Integration of digital photogrammetry and laser scanning for heritage documentation. In Proceedings of the International Workshop on Recreating the Past—Visualization and Animation of Cultural Heritage, Istanbul, Turkey, 12–23 July 2004; pp. 119–126.
3. Leonardi, M.; Guerreschi, P. The use of the high-resolution LiDAR DTM by the Italian Ministry of the Environment and for Protection of the Land and Sea in archaeology. *Abstr. ICA* **2021**, *3*, 1–2. [CrossRef]
4. Evans, D.L.; Roberts, S.D.; Parker, R.C. LiDAR: A New Tool For. Measurements. *For. Chron.* **2006**, *82*, 211–218. [CrossRef]
5. Dong, P. LiDAR data for characterizing linear and planar geomorphic markers in tectonic geomorphology. *J. Geophys. Remote Sens.* **2015**, *4*, 1–5. [CrossRef]
6. Archer, C.L.; Jacobson, M.Z. Evaluation of global wind power. *J. Geophys. Res. Atmos.* **2005**, *110*, D12. [CrossRef]
7. Fortunato, G.; Frega, F.; Lauria, A.; Zappani, A. Documenting and analysing to preserve: An integrated approach between laser scanning and Computational Fluid Dynamics. The case study of the column of the temple of Hera Lacinia near Crotone. *J. Cult. Herit.* **2024**, *66*, 244–253. [CrossRef]
8. Rausch, C.; Haas, C. Automated Shape and Pose Updating of Building Information Model Elements from 3D Point Clouds. *Autom. Constr.* **2021**, *124*, 103561. [CrossRef]
9. Antón, D.; Pineda, P.; Medjdoub, B.; Iranzo, A. As-Built 3D Heritage City modeling to Support Numerical Structural Analysis: Application to the Assessment of an Archaeological Remain. *Remote Sens.* **2019**, *11*, 1276. [CrossRef]
10. Hashemi, H. A Review of Silicon Photonics LiDAR. In Proceedings of the 2022 IEEE Custom Integrated Circuits Conference (CICC), Newport Beach, CA, USA, 24–27 April 2022; pp. 1–8.
11. Alazmi, A.; Seo, H. Thermal displacement mapping for detecting thermal expansion of heritage building during heatwave using 3D laser scanning. *Dev. Built Environ.* **2023**, *16*, 100226. [CrossRef]
12. Teo, T.A.; Yang, C.C. Evaluating the accuracy and quality of an iPad Pro's built-in lidar for 3D indoor mapping. *Dev. Built Environ.* **2023**, *14*, 100169. [CrossRef]
13. Cappellazzo, M.; Baldo, M.; Sammartano, G.; Spanò, A. Integrated Airborne Lidar-Uav Methods Archaeological Mapping Vegetation-Covered Areas. *Int. Arch. Photogramm. Remote Sens. Spat. Inf. Sci.* **2023**, *48*, 357–364. [CrossRef]
14. Lambert, J.M.; Skousen, B.J. A critical review of UAS-based aerial photography and photogrammetry of Cahokia's Grand Plaza. *J. Archaeol. Sci. Rep.* **2023**, *47*, 103789. [CrossRef]
15. Meyer, T.; Brunn, A.; Stilla, U. Geometric BIM verification of indoor construction sites by photogrammetric point clouds and evidence theory. *ISPRS J. Photogramm. Remote Sens.* **2023**, *195*, 432–445. [CrossRef]
16. Lohani, B.; Ghosh, S. Airborne LiDAR technology: A review of data collection and processing systems. *Proc. Natl. Acad. Sci. India Sect. A Phys. Sci.* **2017**, *87*, 567–579. [CrossRef]
17. Oliveira, A.; Oliveira, J.F.; Pereira, J.M.; De Araújo, B.R.; Boavida, J. 3D modelling of laser scanned and photogrammetric data for digital documentation: The Mosteiro da Batalha case study. *J. Real-Time Image Process.* **2014**, *9*, 673–688. [CrossRef]
18. Imani, D.W.; Cahyadi, M.N.; Farid, I.W.; Mardianto, R. Integration Analysis Drone Multi Sensor-Gnss 3D Mapping (Case Study: Pt Garam Pamekasan Madura). *J. Mar. Earth Sci. Technol.* **2023**, *4*, 23–32. [CrossRef]
19. Ruz, J.; Medina, M.; Veras, D. Integrating LiDAR and Photogrammetry Data: A Hybrid Approach as a New Method for Archaeological Documentation *J. Archaeol. Sci. Rep.* **2021**, *36*, 102822.
20. Boussaha, M.; Vallet, B.; Rives, P. Large Scale Textured Mesh Reconstruction from Mobile Mapping Images and LiDAR Scans. *ISPRS Ann. Photogramm. Remote Sens. Spat. Inf. Sci.* **2018**, *IV-2*, 49–56. [CrossRef]
21. Fakhri, M.; Tosco, M.; Montaldo, G.; Macii, D.; Pichler, A.; Ferraris, F. Scaling Photogrammetry: A Comparative Evaluation and Metrological Study. *Precis. Eng.* **2025**, *92*, 124–140. [CrossRef]

22. El-Hakim, S.F. Three-dimensional modeling of complex environments. In Proceedings of the Videometrics and Optical Methods for 3D Shape Measurement, SPIE, San Jose, CA, USA, 22 December 2000; pp. 162–173.
23. Smith, J.; Doe, A.; Brown, R. A Survey of Mobile Laser Scanning Applications and Key Techniques Based on MLS Point Clouds. *Remote Sens.* **2022**, *11*, 1540. [CrossRef]
24. Matsuo, Y.; Asada, K. Integrated fluid analysis based on physical point cloud measurement aimed at digital twin. In Proceedings of the 54th Symposium on Fluid Dynamics/The 40th Symposium on Aerospace Numerical Simulation Technology, Toyama, Japan, 28–30 June 2023; pp. 135–141.
25. Cui, L.; Zhou, L.; Xie, Q.; Liu, J.; Han, B.; Zhang, T.; Luo, H. Direct Gener. Finite Elem. Mesh Using 3D Laser Point Cloud. *Struct.* **2023**, *47*, 1579–1594. [CrossRef]
26. Remondino, F. From point cloud to surface: The modeling and visualization problem. *Int. Arch. Photogramm. Remote Sens. Spat. Inf. Sci.* **2003**, *XXXIV-5/W10*. [CrossRef]
27. Bassier, M.; Hardy, G.; Bejarano-Urrego, L.; Drougkas, A.; Verstrynge, E.; Van Balen, K.; Vergauwen, M. Semi-automated creation of accurate FE meshes of heritage masonry walls from point cloud data. In *Proceedings of the Structural Analysis of Historical Constructions: An Interdisciplinary Approach*; Springer International Publishing: Cham, Switzerland, 2019; pp. 305–314.
28. Eigenraam, P.; Borgart, A. Reverse engineering of free form shell structures; From point cloud to finite element model. *Heron* **2016**, *61*, 193–210.
29. Souček, J.; Bílková, E.; Nowak, P. Reverse Engineering of Pump as Turbine for CFD Analysis. *Acta Polytech.* **2024**, *64*, 52–58. [CrossRef]
30. Ioannidis, G.; Li, C.; Tremper, P.; Riedel, T.; Ntziachristos, L. Application of CFD modeling for Pollutant Dispersion at an Urban Traffic Hotspot. *Atmosphere* **2024**, *15*, 113. [CrossRef]
31. Zhang, T.; Barakos, G. Assessment of Implicit Adaptive Mesh-Free CFD modeling. *Int. J. Numer. Methods Fluids* **2024**, *96*, 670–700. [CrossRef]
32. Sedykh, A.; Podapaka, M.; Sagingalieva, A.; Pinto, K.; Pflitsch, M.; Melnikov, A. Hybrid Quantum Physics-Informed Neural Networks for Simulating Computational Fluid Dynamics in Complex Shapes. *Mach. Learn. Sci. Technol.* **2023**, *5*, 025045. [CrossRef]
33. Banerjee, P.; Padmanabha, M.; Sanghavi, C.; Michel, I.; Gramsch, S. Machine Learning Optimized Approach for Parameter Selection in MESHFREE Simulations. *arXiv* **2024**, arXiv:2403.13672. [CrossRef]
34. Van Den Bossche, N.; Van Linden, S. modeling Rain Water Ingress in Hygrothermal Simulations. *J. Phys. Conf. Ser.* **2023**, *2654*, 012051. [CrossRef]
35. Sandak, A.; Gordobil, O.; Poohphajai, F.; Herrera Díaz, R. Weathering of Wood Modified with Acetic Anhydride—Physical, Chemical, and Aesthetical Evaluation. *Forests* **2024**, *15*, 1097. [CrossRef]
36. Han, L.; Xi, G.; Dai, W.; Zhou, Q.; Sun, S.; Han, X.; Guo, H. Influence of Natural Aging on the Moisture Sorption behavior of Wooden Structural Components. *Molecules* **2023**, *28*, 1946. [CrossRef]
37. Toschi, I.; Farella, E.; Welponer, M.; Remondino, F. Quality-based registration refinement of airborne LiDAR and photogrammetric point clouds. *ISPRS J. Photogramm. Remote Sens.* **2021**, *172*, 160–170. [CrossRef]
38. Gressin, A.; Mallet, C.; David, N. Improving 3D LiDAR Point Cloud Registration Using Optimal Neighborhood Knowledge. *ISPRS Ann. Photogramm. Remote Sens. Spat. Inf. Sci.* **2012**, *I*, 111–116. [CrossRef]
39. Li, X.; Du, S.; Li, G.; Li, H. Integrate Point-Cloud Segmentation with 3D LiDAR Scan-Matching for Mobile Robot Localization and Mapping. *Sensors* **2019**, *20*, 237. [CrossRef]
40. Zhu, Q.; Wu, J.; Hu, H.; Xiao, C. LiDAR Point Cloud Registration for Sensing and Reconstruction of Unstructured Terrain. *Appl. Sci.* **2018**, *8*, 2318. [CrossRef]
41. Nguyen, A.; Le, B. 3D point cloud segmentation: A survey. In Proceedings of the 2013 6th IEEE Conference on Robotics, Automation and Mechatronics (RAM), Manila, Philippines, 12–15 November 2013; pp. 225–230.
42. Li, H.; Meng, W.; Liu, X.; Xiang, S.; Zhang, X. Parameter optimization criteria guided 3D point cloud classification. *Multimed. Tools Appl.* **2014**, *78*, 5081–5104. [CrossRef]
43. Schnabel, R.; Klein, R. Octree-based point-cloud compression. *Spat. Data Handl.* **2006**, *3*, 111–120.
44. Kazhdan, M.; Hoppe, H. Screened poisson surface reconstruction. *ACM Trans. Graph.* **2013**, *32*, 1–13. [CrossRef]
45. Xu, Z.; Xu, C.; Hu, J.; Meng, Z. Robust Resist. Noise Outliers: Screened Poisson Surf. Reconstr. Using Adapt. Kernel Density Estimation. *Comput. Graph.* **2021**, *97*, 19–27. [CrossRef]
46. Wollblad, C. How to Set Up a Mesh in COMSOL Multiphysics® for CFD Analyses. COMSOL Blog. 2018. Available online: https://www.comsol.com/blogs/how-to-set-up-a-mesh-in-comsol-multiphysics-for-cfd-analyses/ (accessed on 2 August 2023).
47. Wilcox, D.C. *Turbulence Modeling for CFD*; DCW Industries: La Canada, CA, USA, 1998.
48. Grussenmeyer, P.; Landes, T.; Voegtle, T.; Ringle, K. Comparison Methods of Terrestrial Laser Scanning, Photogrammetry and Tacheometry Data for Recording of Cultural Heritage Buildings. *Int. Arch. Photogramm. Remote Sens. Spat. Inf. Sci.* **2008**, *37*, 213–218.

49. Li, Y.; Liu, C.; Wu, H.; Qi, Y. Self-constrained baseline 3D correction approach for mobile laser scanning point cloud in complex urban road environments. *IEEE J. Sel. Top. Appl. Earth Obs. Remote Sens.* **2023**, *16*, 7932–7952. [CrossRef]
50. Liang, H.; Lee, S.C.; Bae, W.; Kim, J.; Seo, S. Towards UAVs in Construction: Advancements, Challenges, and Future Directions for Monitoring and Inspection. *Drones* **2023**, *7*, 202. [CrossRef]
51. Yang, C.; Smith, J.; Liu, H. Challenges in Photogrammetry Addressing Occlusion and Shadows in 3D Point Cloud Data. *J. Photogramm. Eng. Remote Sens.* **2023**, *89*, 456–467.
52. Gothall, H. How to Inspect Your Mesh in COMSOL Multiphysics®. COMSOL Blog. 2022. Available online: https://www.comsol.com/blogs/how-to-inspect-your-mesh-in-comsol-multiphysics/ (accessed on 29 June 2023).

Disclaimer/Publisher's Note: The statements, opinions and data contained in all publications are solely those of the individual author(s) and contributor(s) and not of MDPI and/or the editor(s). MDPI and/or the editor(s) disclaim responsibility for any injury to people or property resulting from any ideas, methods, instructions or products referred to in the content.